Progress In Electromagnetics Research C, Vol. 161, 56–65, 2025

PIER C

(Received 8 August 2025, Accepted 15 October 2025, Scheduled 27 October 2025)

Research on Control of Wireless Power Transfer System Based on Switched Inductor

Zhongjiu Zheng, Yanpeng Ma*, Zhilong Wu, Xingfeng Cao, Qiangqiang Zhao, and Fuyu Song

College of Marine Electrical Engineering, Dalian Maritime University, Dalian 116026, China

ABSTRACT: During the vehicle parking process, the misalignment between transmitting and receiving coils caused by different parking positions results in variations in the system's mutual inductance. These variations compromise system performance and stability. To address this challenge, this study proposes a control strategy for a wireless power transfer system utilizing switched inductors. First, an efficiency optimization method based on tunable inductors is introduced in detail. This method eliminates the need for bilateral communication or additional hardware. By dynamically adjusting the switched inductor values, the system maintains optimal load conditions across various topologies. Furthermore, switched capacitors are employed to achieve system resonance tuning. Second, a phase-shift control strategy is implemented to ensure efficient system operation while maintaining constant voltage output. Finally, an experimental prototype is constructed to validate the proposed approach. Experimental results demonstrate that the proposed control method achieves a constant output voltage of 24 V with system efficiency exceeding 81%.

1. INTRODUCTION

In recent decades, wireless power transfer (WPT) technology has garnered significant attention and adoption across diverse applications owing to its high reliability, safety, and elimination of physical connectors. It has been extensively employed in areas such as biomedical implants [1], wireless charging for mobile devices [2], electric vehicle (EV) charging systems [3], unmanned aerial vehicles [4], and autonomous underwater vehicles (AUVs) [5].

Particularly in EV charging applications, variations in parking position often lead to the misalignment between transmitting and receiving coils. This misalignment results in fluctuations in mutual inductance, which in turn adversely affects the power transfer efficiency and output voltage stability of the system. Consequently, enhancing the misalignment tolerance of WPT systems has become a critical research focus, aiming to maintain consistent performance under realistic operating conditions.

In order to maintain the efficient operation of the system, the current methods can be divided into the following three categories [6, 7]. 1) power converter [8, 9]; 2) frequency switching [10, 11]; 3) Parameter adjustment [12, 13].

1) Power converter. Maximum efficiency tracking (MET) of the system is accomplished via a DC/DC converter or an active rectifier. The authors of [8] adjust the duty cycle of the DC/DC converter to tune the system load to its optimal equivalent load; notably, the system efficiency remains above 75 % even when the coil offset reaches 200 mm. In [9], researchers realize pulse-density modulation through a delta-sigma modulator to further regulate the active rectifier, enabling the system to maintain both constant-voltage (CV) output and overall efficiency above 70% under a wide range of offset conditions. However, the aforementioned methods necessitate the integration of additional hardware components, thereby occupying extra space. Consequently, their applicability becomes limited in scenarios requiring extended driving ranges for vehicles.

2) Frequency switching. The authors of [10] utilize frequency-modulated phase-shift keying communication technology to integrate electrical information from transmitting and receiving sides, deriving the system's optimal operating frequency. Subsequently, by adjusting the frequency, they maintain the system efficiency above 93% even under significant offset conditions. The work in [11] demonstrates that the primary side employs spread-spectrum technology to vary the inverter's operating frequency, whereas the secondary side uses synchronous current control (SCC) to rapidly track the system's operating frequency, thereby enhancing the system efficiency by 7–13%.

3) Parameter adjustment. The authors of [12] derive the capacitance value required to achieve maximum efficiency via mathematical analysis. They then reduce the system's reactive power by adjusting the conduction angle of the bilateral switched capacitor in real time, thereby maintaining the system efficiency above 87%. In [13], researchers demonstrate that bilateral independent control can be used to tune the switching capacitor size, allowing the system to remain in a resonant state consistently — *without the need for communication* — and resulting in a 3% improvement in system efficiency. Notably, the aforementioned methods rely either on bilateral communication or bilateral independent control. On the one hand, communication introduces additional costs; on the other hand, bilateral control increases the overall control complexity of the system.

---

* Corresponding author: Yanpeng Ma (m2802269239@dlmu.edu.cn).

doi:10.2528/PIERC25080801

Published by THE ELECTROMAGNETIC ACADEMY

On the one hand, the above three methods require bilateral communication or independent control, which increases the difficulty of system control. On the other hand, the additional circuit needs to occupy more system volume, which is not conducive to the long-range operation of car [14]. Therefore, an efficient maximum efficiency tracking control method is needed. At the same time, the above method only analyzes the efficiency caused by offset and does not take into account the fluctuation of the system output voltage with offset.

CV control strategies can be categorized into transmitter-side and receiver-side control methods based on the controller's placement [15]. For space-constrained electrical systems such as vehicles, the transmitter-side control strategy is preferable to its receiver-side counterpart [16]. Transmitter-side CV output control can be classified into four categories: 1) DC/DC converters [17, 18]; 2) Frequency switching [19, 20]; 3) Phase-shift control [21, 22].

1) DC/DC converter [17, 18]. With this method, the system must acquire the current mutual inductance and load values, then utilize mathematical analysis and related techniques to derive the relationship among the output voltage, these two parameters, and the input voltage. Subsequently, output voltage regulation is achieved by adjusting the duty cycle of the DC/DC converter. However, this approach necessitates additional circuitry, which increases system cost and volume.

2) Frequency switching [19, 20]. Through systematic parameter design, the system exhibits load-independent CV output characteristics across different frequencies. Furthermore, system CV charging control is achieved by adjusting the operating frequency.

3) Phase shift control [21, 22]. Using the parameter identification method, the required system parameters such as mutual inductance are obtained, and the current output voltage of the system is further estimated without communication. According to the function of the conduction angle and output voltage, the conduction angle is adjusted to realize the CV charging control of the system.

Compared with [8, 9], the efficiency tracking process in this paper does not require additional DC/DC converters, which reduces the system volume and hardware costs. Compared with [10, 11], this paper does not need to adjust the system operating frequency, which facilitates the stable operation of the system. Compared with [12, 13], this paper requires no bilateral communication and only needs transmitter-side control. This not only eliminates the hardware costs of bilateral communication and avoids the issue of communication susceptibility to interference, but also results in a higher overall error tolerance rate and is more conducive to accurate implementation. Compared with [17–22], this paper implements CV charging while performing MET, which helps maintain efficient constant voltage charging of the system. Therefore, the main contributions of this paper are summarized and explained as follows:

1) A switched inductor-based efficiency control method is proposed, which does not require additional devices or bilateral communication, greatly reducing the system cost and control difficulty.

2) The efficiency control method is applicable to various topologies. The optimal load of different topologies can be derived from Kirchhoff's laws, thus it has good universality.

3) Phase-shift control and capacitor adjustment are adopted to keep the system in a resonant state and enable CV output with maximum efficiency, which is conducive to the efficient and stable operation of the system.

The rest of this article is as follows. The second section introduces the working principle of the system and briefly analyzes the working principle of the current parameter identification. The third section introduces the MET process and CV output control method, and analyzes its working principle in detail. The fourth section verifies the feasibility of the method through experimental results. Finally, the fifth section summarizes the full text.

2. WPT SYSTEM AND PARAMETER IDENTIFICATION

In the previous research of AUV CV output and MET control, the transmitting side control strategy relies on the wireless communication module to feed the charging information back [25]. In order to reduce the cost and complexity of the system, the wireless communication module can be replaced by the primary side parameter identification [26]. Therefore, this paper chooses to carry out non-communication control on the transmitting side. The LCC-S topology is widely used because of its load-independent CV output characteristics [27]. Therefore, the LCC-S topology shown in Fig. 1 is selected in this paper. It consists of four Metal-Oxide-Semiconductor Field Effect Transistors (MOSFETs) to form a full-bridge inverter, which is used to invert the DC power supply voltage U_{in} into a high-frequency square wave voltage U_1. Further power is transmitted from transmitting coil L_p to receiving coil L_s, and finally the DC output voltage U_{out} is generated by the rectifier to charge the load.

The research focus of this paper is to realize the system CV output while realizing the system MET when the mutual inductance is known. In our previous work [24], the current mode equation can be used to realize the mutual inductance parameter identification without communication. Therefore, we take it as the basis and briefly introduce it below. If other non-communication mutual inductance parameter identification methods are used, the CV output and MET control of this paper can still be realized.

In order to facilitate the system analysis, the equivalent circuit is shown in Fig. 2. The compensation capacitance and inductance of the transmitting side are both variables, so they are expressed as C_{P_var} and L_{1_var}. C_1 and C_s are compensation capacitors. The mutual inductance between the coils is M; R_{L1}, R_{Lp}, and R_{Ls} are the parasitic resistance of each coil, and the load is R_L. According to [28], the circuit parameters are designed by (1) to achieve efficient operation of the system, where ω is the resonant frequency. The equivalent voltage source U_1 and equivalent load R are shown in (2) and (3), where α is the conduction angle of the inverter.

$$\omega = \frac{1}{\sqrt{L_1 C_1}} = \frac{1}{\sqrt{L_s C_s}} = \frac{1}{\sqrt{(L_p - L_1)\, C_p}} \tag{1}$$

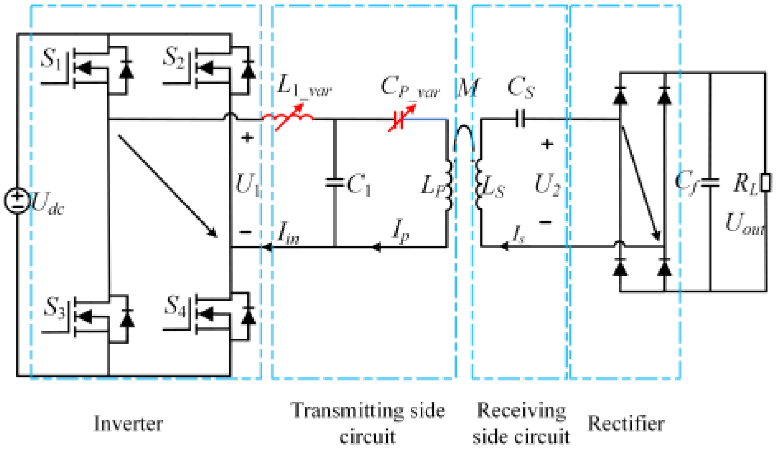

FIGURE 1. Circuit model of WPT system.

$$U_1 = \frac{2\sqrt{2}}{\pi} U_{in} \sin\frac{\alpha}{2} \tag{2}$$

$$R = \frac{8}{\pi^2} R_L \tag{3}$$

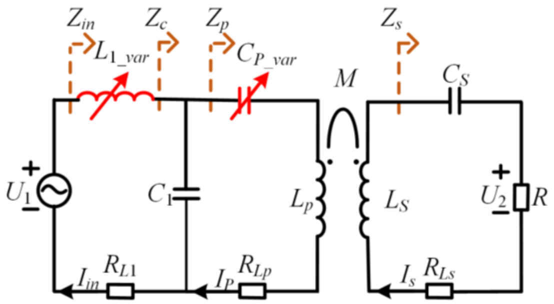

FIGURE 2. LCC-S equivalent circuit.

Starting from Fig. 2, the system input current modulus $|I_{in}|$ is shown in (4), where M is the parameter to be identified.

$$|I_{in}| = f(M) = \frac{U_{in}}{\sqrt{X_{in}^2 + R_{in}^2}} \tag{4}$$

Based on trigonometric function, the current modulus is equal to the effective value, so the mutual inductance M can be identified by bringing the measured current effective value I_{in_mea} into (4). Because it has only one solution, the traditional numerical solution method can be replaced by particle swarm optimization and other methods to achieve simple parameter identification. So far, the required M has been obtained. The accuracy of the above identification method has been discussed and verified in our previous work, and it is no longer repeated here.

On this basis, according to Kirchhoff's theorem, the circuit equation is written as follows:

$$\begin{cases} U_1 = (R_{L1} + j\omega L_{1\_var})\, I_{inr} + (R_{Lp} + j\omega L_p \\ \qquad + \frac{1}{j\omega C_{P\_var}}\Big)\, I_p + j\omega M I_s \\ \left(R_{Lp} + j\omega L_p + \frac{1}{j\omega C_{p\_var}}\right) I_p + j\omega M I_s = \frac{1}{j\omega C_1}(I_{in} - I_p) \\ -RI_s = \left(R_{Ls} + j\omega L_s + \frac{1}{j\omega C_s}\right) I_s + j\omega M I_p \end{cases} \tag{5}$$

Therefore, the output voltage and efficiency of the equivalent circuit are as follows:

$$\begin{cases} U_2 = \frac{\omega^2 L_{1\_var} M U_1 R}{\omega^2 M^2 R_{L1} + (R + R_{Ls})(\omega^2 L_{1\_var}^2 + R_{L1} R_{Lp})} \\ A = \omega^4 M^4 R_{L1} + (R + R_{Ls})^2 (\omega^2 L_{1\_var}^2 R_{Lp} + R_{L1} R_{Lp}^2) \\ \eta = \frac{\omega^4 L_{1\_var}^2 M^2 R}{(R + R_{Ls})(\omega^4 L_{1\_var}^2 M^2 + 2\omega^2 M^2 R_{L1} R_{Lp}) + A} \end{cases} \tag{6}$$

For the output voltage of the system, since the voltage before the rectifier bridge is a square wave, the expression is shown in (7):

$$U_{out} = \frac{\pi\sqrt{2}}{4} U_2 \tag{7}$$

For system efficiency, when the system reaches the maximum efficiency, the corresponding R is the optimal equivalent load R_{opt}. Therefore, find the derivative of R for (6), and let its derivative be 0. R_{opt} is obtained as shown in (8):

$$B = \left(R_{Lp}\omega^2 L_{1\_var}^2 + R_{L1}\omega^2 M^2 + R_{L1} R_{Lp} R_{Ls}\right)$$

$$R_{opt} = \frac{\sqrt{R_{Lp}(\omega^2 L_{1\_var}^2 + R_{L1} R_{Lp})\,(\omega^2 M^2 + R_{Lp} R_{Ls}) B}}{R_{Lp}\omega^2 L_{1\_var}^2 + R_{L1} R_{Lp}^2} \tag{8}$$

Therefore, it can be seen from (6)–(8) that when the system parameters are fixed, with the fluctuation of M caused by the offset, the system output voltage and optimal load value will also fluctuate, which is not conducive to the efficient and stable operation of the system. Therefore, in order to solve the above problems, this paper adopts the control method of switching inductance and fast calculation of conduction angle to improve the anti-offset ability of the system.

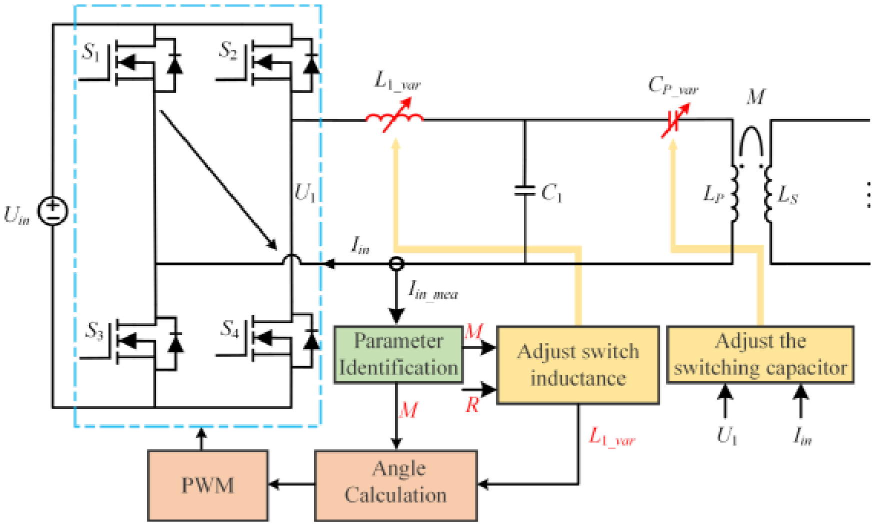

FIGURE 3. Control flowchart.

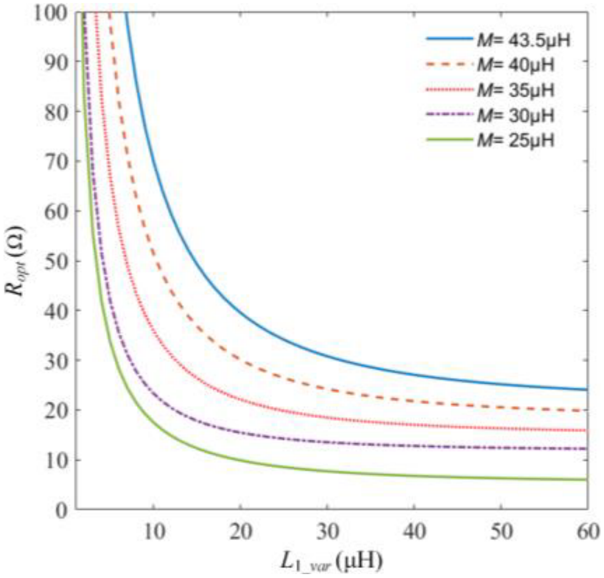

FIGURE 4. R_{opt} varies with M and L_{1_var}.

3. CV OUTPUT AND MET CONTROL BASED ON PARAMETER IDENTIFICATION

In order to make the system work in the case of Ropt to achieve CV charging control, this paper adopts the CV output and MET control method based on mutual inductance parameter identification, and the control diagram is shown in Fig. 3. The working principle is as follows. Firstly, the input electrical information is collected for parameter identification. Secondly, the switching inductance L_{1_var} is adjusted according to the identification results to make the current load of the system become R_{opt}, and the system is in a resonant state by adjusting the capacitance C_{P_var}. Finally, the CV charging control of the system is realized by using the method of fast calculation of the conduction angle.

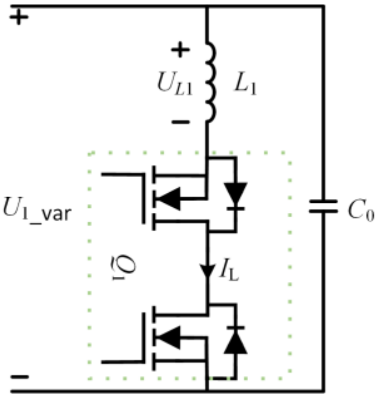

FIGURE 5. Topological structure of switching inductor.

3.1. MET Based on Switching Inductance

When the system parameters are fixed, according to (8), if M is known, then R_{opt} is only related to L_{1_var}, and the relationship between L_{1_var} and R_{opt} is shown in Fig. 4.

In Fig. 4, when M remains constant, as L_{1_var} changes, R_{opt} will also change, and the two are one-to-one correspondence. Therefore, this paper adopts the method of adjusting L_{1_var} to make the current equivalent load R of the system into R_{opt}. The principle of the method is to make the system work under R_{opt} by adjusting the turn-off angle of the switching inductance. That is, if the current load is 30 Ω, by adjusting L_{1_var}, let R_{opt} be 30 Ω. If it is other resistance values, the adjustment method is similar, and the relationship among the three is shown in (9):

$$R_{opt} = f\left(L_{1\_var}\right) = R \tag{9}$$

The switched inductor L_{1_var} topology selected in this paper is shown in Fig. 5. It consists of inductor L_1 connected in series with switch Q_1, which is then connected in parallel with capacitor C. Herein, a C is connected in parallel across the L_1 branch, which can effectively reduce the impact of harmonic currents

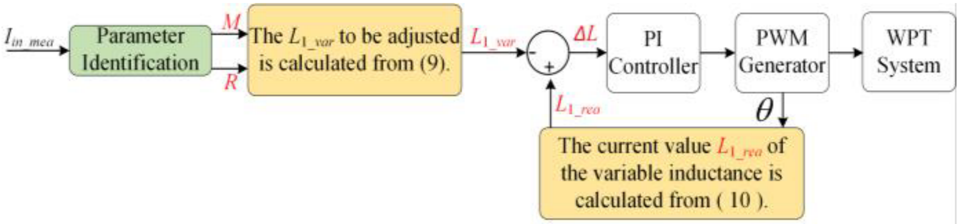

FIGURE 6. Control waveforms of the variable inductor.

generated by the switch on the circuit. Furthermore, the equivalent inductance value of L_{1_var} can be expressed as [29]:

$$L_{1\_var} = \frac{\pi L_1}{\pi - \sin\theta - \theta - \pi\omega^2 C_0 L_1} \tag{10}$$

Therefore, it can be known from (10) that the adjustment of the equivalent inductance can be achieved by changing the turn-off angle θ. Furthermore, the flowchart of the variable inductor is shown in Fig. 6, and its basic working principle is as follows. By collecting the effective value of the system I_{in_mea}, the parameter identification of M is realized. On this basis, the Proportional Integral (PI) module adjusts the Pulse Width Modulation (PWM) according to the error between the target adjustment value of the switched inductor and the current inductance value, thereby realizing the adjustment of θ and ultimately achieving the change of L_{1_var}. It is worth noting that the method in this paper can be applied not only in LCC/S topology but also in other topologies. The R_{opt} of other topologies can be obtained according to Kirchhoff's laws, so it has high applicability.

3.2. System Tuning Based on Switched Capacitor

To effectively address system detuning issues caused by changes in the switched inductor under a fixed frequency, we adopt a switched capacitor topology to achieve system tuning [30]. Its topology is shown in Fig. 7, and the equivalent capacitance value of C_{p_var} can be expressed as [29]:

$$C_{P\_var} = \frac{C_{P1}\pi(C_{P1}+C_{P2})}{\pi(C_{P1}+C_{P2}) - (\theta_1 + \sin\theta_1)C_{P2}} \tag{11}$$

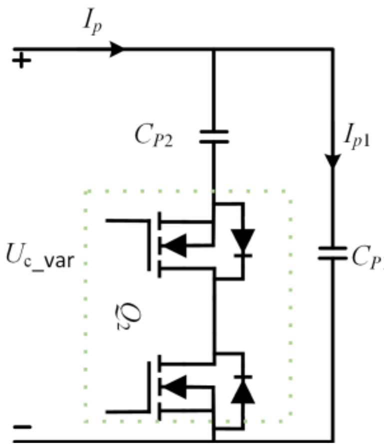

FIGURE 7. Topological structure of switching capacitor.

Therefore, it can be seen from (11) that the adjustment of C_{p_var} can be realized by changing the conduction angle θ_1. When the system is in a resonant state, the imaginary part of the input impedance of the system should be zero, that is, U_1 and I_{in} are in phase [31]. Therefore, based on this, the phase difference θ_2 between U_1 and I_{in} is obtained by using a phase comparator, and then the PWM is controlled by PI to control C_{p_var}, so that the system is in a resonant state. The overall process is shown in Fig. 8.

3.3. Constant Voltage Output Control

When the system realizes MET and tuning, the CV charging control is realized by using the fast calculation of the conduction angle. Combining (2) and (6), (12) can be obtained, which is the relationship between U_{in} and U_2. Combining (7) and (12), (13) can be obtained, which is the relationship between α and output voltage U_{out}. Here, α is the size of the conduction angle required for CV output in the case of M perturbation.

$$U_2 = \frac{2\sqrt{2}\omega^2 L_{1\_var} M R U_{in} \sin\frac{\alpha}{2}}{\pi\left[\omega^2 M^2 R_{L1} + (R+R_{Ls})(\omega^2 L_{1\_var}^2 + R_{L1}R_{Lp})\right]} \tag{12}$$

$$\begin{cases} D = (R+R_{Ls})(\omega^2 L_{1\_var}^2 + R_{L1}R_{Lp}) \\ \alpha = \arcsin\frac{U_{out}\left[\omega^2 M^2 R_{L1} + D\right]}{\omega^2 L_{1\_var} M R U_{in}} \end{cases} \tag{13}$$

Furthermore, the relationship between U_{out} and (M, α) is obtained by (13) as shown in Fig. 9. In Fig. 9(a), the red plane represents the 24 V target output voltage, and the blue surface is the relationship between U_{out} and (M, α). The black intersection line is the intersection line of two surfaces. Further, project it onto the plane (M, α), and the result is shown in Fig. 9(b). In Fig. 9(b), when the output voltage is constant, M fluctuates, and α will also change, The two correspond to each other. Therefore, adjusting α can realize the CV output control of the system.

In summary, the flowchart of the methods in this paper is shown in Fig. 10. The workflow of this paper is as follows:

1) The input current I_{in} is collected to identify M;

2) The identification results are brought into (9) and (10), and the L_{1_var} is adjusted to realize the system MET;

3) The phase difference is collected; the C_{p_var} is adjusted; the system tuning is realized; the C_{p_var} and L_{1_var} are brought back to the identification process to update the parameters;

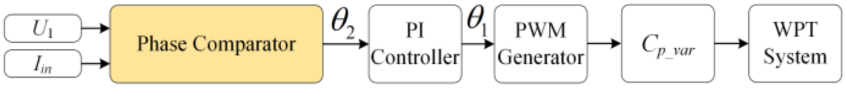

FIGURE 8. Control flow chart for the variable capacitor.

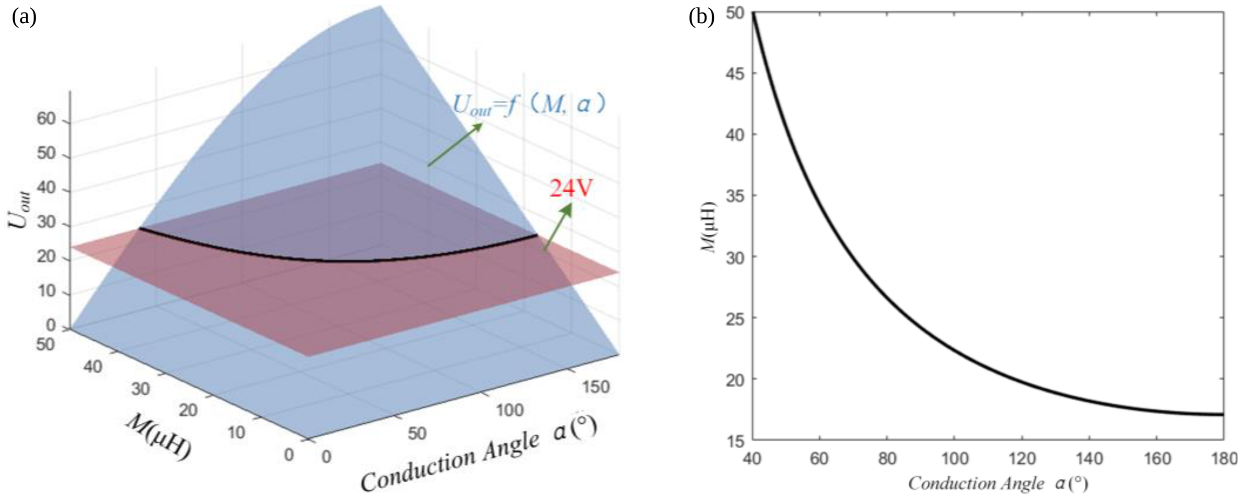

FIGURE 9. The relationship between the U_{out} and (M, α). (a) Three-dimensional graph under 24 V constraint. (b) Top view under the constraint of 24 V.

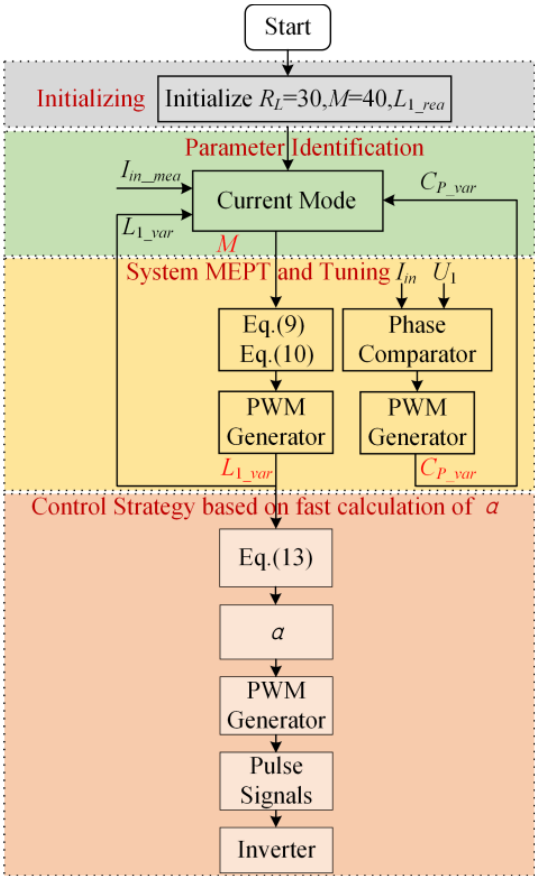

FIGURE 10. Control flow chart.

4) Bring M and L_{1_var} into (13), adjust α, and realize CV output control of the system.

4. EXPERIMENTAL VERIFICATION

Using the experimental parameters listed in Table 1, an experimental platform (Fig. 11) was constructed to validate the feasibility of the proposed method. The platform comprises a DC power supply module, a single-phase bridge inverter consisting of four HL3400 power switches with low on-resistance ($Ron = 0.021\,\Omega$), a digital signal processing (DSP) control unit, a compensation network, a data acquisition module, a switched inductor, and a switched capacitor (The switching device used is STP13NM60N, which has the advantages of high voltage resistance, fast switching speed, and low cost), transmitting and receiving coils, an uncontrolled rectifier bridge composed of four SBDF4060TCTB Schottky diodes with low forward voltage drop ($V_F = 0.52$ V at a 20 A input current), an electronic load provided by the IT8512A, and other auxiliary components.

TABLE 1. Electrical parameters of the system.

Symbol	Quantity	Value
L_p, L_s	self-inductance	146 µH, 146 µH
C_{p_var}	switched capacitor	20–40 nF
C_1, C_s	resonant capacitor	103 nF, 24 nF
L_{1_var}	switched inductor	10–55 µH
R_L	load	30 Ω
U_{in}	input voltage	48 V
f	frequency	85 kHz

In addition, both the transmitting and receiving coils have a diameter of 120 mm and 27 turns. The primary coil is fixed, while the secondary coil can be horizontally offset relative

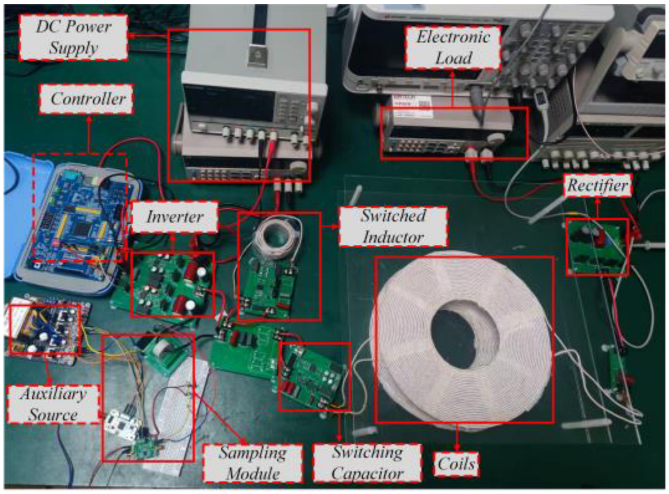

FIGURE 11. Experimental platform.

to the primary coil at various distances. The offset distance ranges from 0 to 65 mm (exceeding the coil radius within this range), with the corresponding mutual inductance varying from 43.5 µH to 22 µH. The load fluctuation range is set to 25 Ω to 40 Ω.

4.1. MET Verification

Prior to system operation, an LCR meter was used to characterize the parameters of the compensation network and coils. For varying coil offsets, the measured variation curve of the system's M is presented in Fig. 12. As clearly illustrated in Fig. 12, mutual inductance decreases monotonically with increasing coil offset. Furthermore, as established earlier, a reduction in mutual inductance leads to decreased efficiency and output voltage fluctuations. Thus, real-time control is necessary to maintain both system efficiency and CV output.

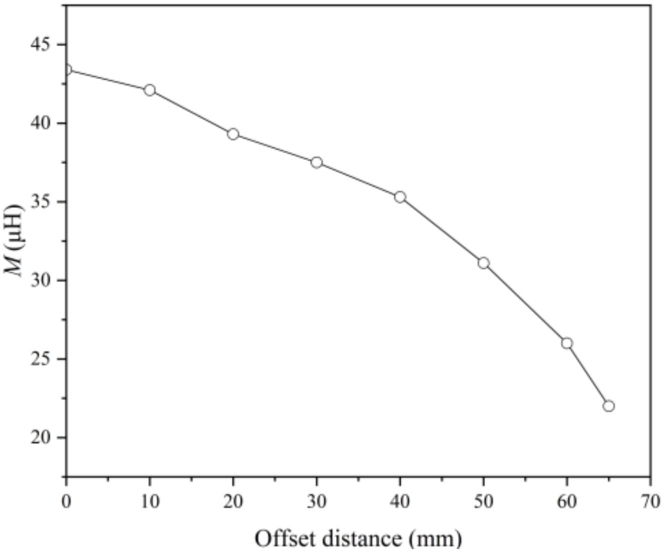

FIGURE 12. Curve of M varying with offset distance.

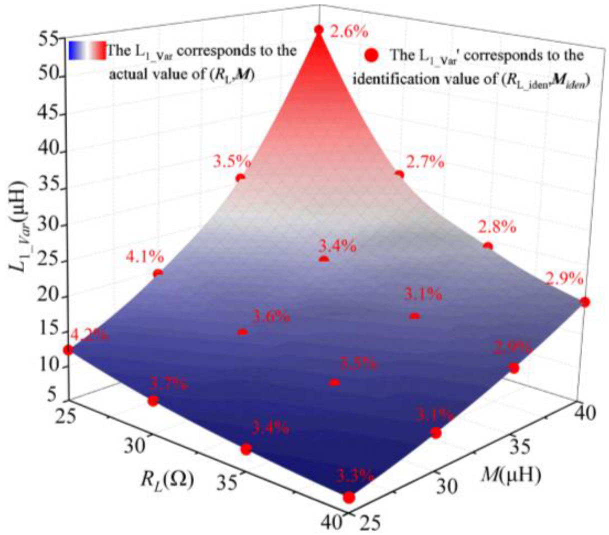

FIGURE 13. The comparison between the identification value and the reference value under different (M, R_L) conditions.

Under varying (M, R_L) conditions, mutual inductance identification results were obtained using the parameter identification method detailed in Section 2. Based on these identification results, L_{1_var} was computed to achieve equivalent load adjustment. The relationship among these three parameters is depicted in Fig. 13. The surface plot in Fig. 13 represents the relationship between the actual (M, R_L) values and L_{1_var}. Red dots denote L_{1_var} values computed from the identified $(M_{\_iden}, R_{L\_iden})$ results, while red numbers indicate the L_{1_var} identification error. Notably, the error between the two is within 4.2%. Potential sources of this error include inaccuracies in acquired electrical data and self-inductance fluctuations during coil offset.

Figure 14 presents system efficiency variation under different load and mutual inductance conditions. Here, the orange bars represent the efficiency when both the switched inductor and switched capacitor are used, while the green bars correspond to the uncontrolled case. As observed in Fig. 14(a), with a load of 30 Ω, the red curve is consistently higher than the blue curve; this differential becomes more pronounced as M decreases, reaching a maximum of 18%. Similarly, Fig. 14(b) demonstrates that with a 40 Ω load, the proposed control strategy improves system efficiency by 15%.

Furthermore, Fig. 15 shows the system input voltage and current waveforms under tuned and untuned conditions. Notably, in the absence of switched capacitor control, the system operates in a detuned state, which results in increased reactive power and subsequent reduction in system efficiency. With the implementation of switched capacitor control, the system maintains a resonant state, facilitating sustained efficient operation.

4.2. CV Output

The proposed method was experimentally validated under horizontal coil offsets ranging from 70 mm to 80 mm, with results presented in Fig. 16. Fig. 16 illustrates variations in the system's electrical parameters as mutual inductance decreases

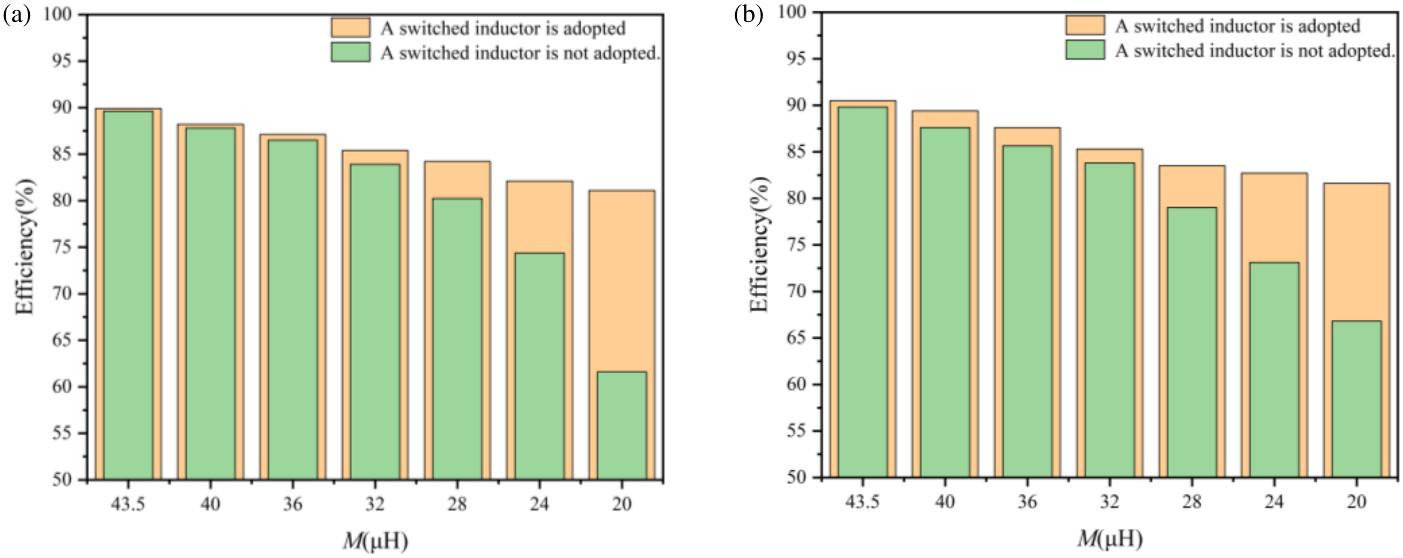

FIGURE 14. System efficiency comparison: (a) $R_L = 30\,\Omega$; (b) $R_L = 40\,\Omega$.

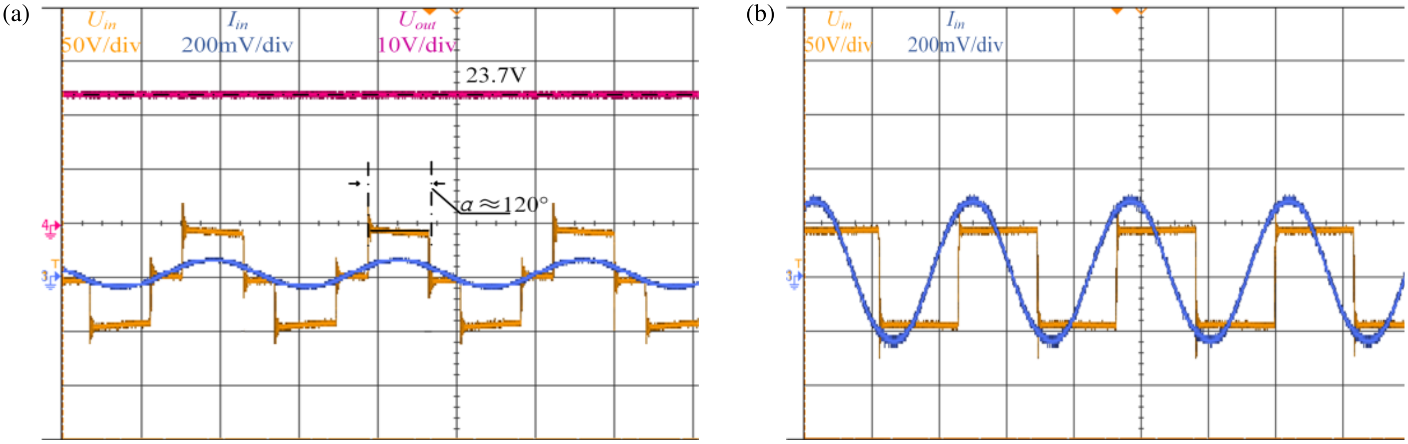

FIGURE 15. When $M = 38\,\mu\text{H}$, $L_{1\_var} = 27.2\,\mu\text{H}$, the system input voltage and current curves under different capacitances. (a) $C_{p\_var} = 29.5\,\text{nF}$; (b) $C_{p\_var} = 30.8\,\text{nF}$.

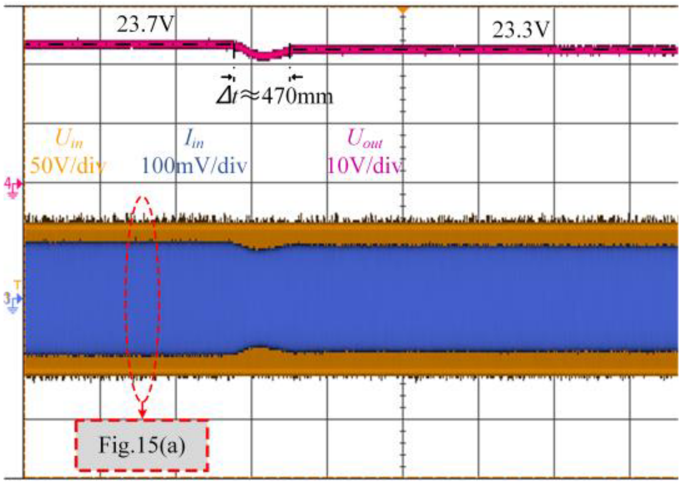

FIGURE 16. The variation curve of the system's electrical information when $R_L = 30\,\Omega$ and M changes from $38\,\mu\text{H}$ to $30\,\mu\text{H}$.

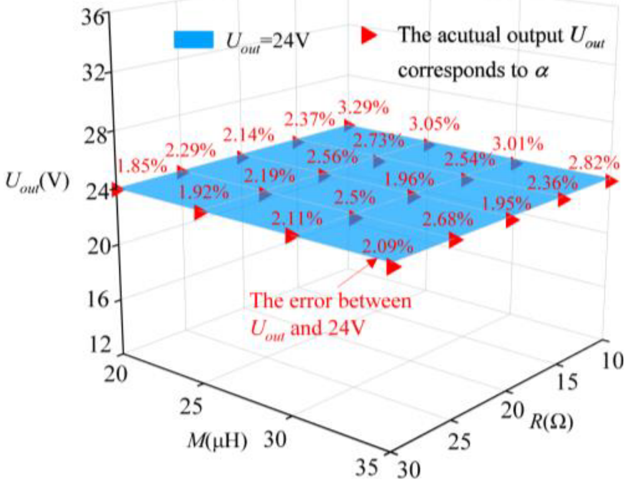

FIGURE 17. The output voltage of the proposed control strategy is compared with the 24 V output voltage.

from 38 μH to 30 μH. Here, the purple line represents the load charging voltage, while the orange and blue curves correspond to the inverter's input voltage and current, respectively. As observed, the system voltage changes from 23.7 V to 23.3 V during coil offset, with the overall voltage fluctuation rate within 3%. Additionally, Fig. 15(a) depicts the electrical parameter variations at a mutual inductance of 38 μH; as shown, the system achieves constant-voltage output by adjusting the conduction angle to 120°.

Furthermore, Fig. 17 presents the system output voltage under various offset conditions. In this figure, red triangles denote the measured output voltage values; the blue plane represents the 24 V constant-voltage reference plane; and red numbers indicate output voltage errors. Notably, the overall output voltage fluctuation is controlled within 3%, fully confirming the feasibility of the proposed method.

5. CONCLUSION

To improve the anti-offset performance of WPT systems, this paper proposes a switched-inductor-based control strategy for WPT systems. Based on parameter identification results, the proposed method tunes the switched inductor to achieve MET and adjusts the switched capacitor to maintain the system in a resonant state — reducing reactive power and thereby sustaining system efficiency above 80%. Additionally, a rapid conduction angle calculation method is employed to realize 24 V CV output control with voltage fluctuations within 3%. Thus, the proposed method effectively enhances the system's anti-offset performance and provides a viable solution for high-efficiency constant-voltage control in WPT systems. Due to the limitations of experimental equipment, in the future, we will further conduct research on higher power, optimize the magnetic coupler and cooling mechanism, and adopt wide-bandgap devices (SiC/GaN) to improve efficiency and reduce thermal stress.

ACKNOWLEDGEMENT

The corresponding author, on behalf of all authors, acknowledges the support for this paper from the Fundamental Research Funds for the Central Universities (Grant No. 3132025616).

REFERENCES

[1] Mukherjee, D., S. K. Rainu, N. Singh, and D. Mallick, "A miniaturized, low-frequency magnetoelectric wireless power transfer system for powering biomedical implants," *IEEE Transactions on Biomedical Circuits and Systems*, Vol. 18, No. 2, 438–450, Apr. 2024.

[2] Yu, X., J. Feng, L. Zhu, and Q. Li, "Design and optimization of a planar omnidirectional wireless power transfer system for consumer electronics," *IEEE Open Journal of Power Electronics*, Vol. 5, 311–322, 2024.

[3] Jo, C.-H. and D.-H. Kim, "Simplified integration of bidirectional OBC and WPT charging systems with reconfiguring topology for electric vehicles," *IEEE Transactions on Power Electronics*, Vol. 40, No. 6, 7651–7656, Jun. 2025.

[4] Lv, X., X. Dai, F. Yu, X. Li, H. Wang, Y. Sun, and J. Hu, "A high misalignment tolerance SCC-WPT system with relay single capacitive coupler for UAV wireless charging applications," *IEEE Transactions on Power Electronics*, Vol. 40, No. 8, 10 372–10 377, Aug. 2025.

[5] Wang, Z., X. Liu, F. Gao, Y. Jiang, H. Li, Y. Liu, Z. Cheng, and Y. Zhang, "An optimization approach for efficiency and interoperability enhancement of WPT systems for autonomous underwater vehicles," *IEEE Transactions on Power Electronics*, Vol. 40, No. 4, 6345–6358, Apr. 2025.

[6] Yang, H., Y. Li, J. Chen, Y. Shao, Z. Yan, R. Mai, and Z. He, "A hybrid load matching method for WPT systems to maintain high efficiency over wide load range," *IEEE Transactions on Transportation Electrification*, Vol. 9, No. 1, 1993–2005, Mar. 2023.

[7] Yakala, R. K., D. P. Nayak, and S. K. Pramanick, "Input reactive power control of bidirectional WPT to improve system efficiency," *IEEE Transactions on Industry Applications*, Vol. 60, No. 4, 5813–5824, Jul.-Aug. 2024.

[8] Li, H., J. Li, K. Wang, W. Chen, and X. Yang, "A maximum efficiency point tracking control scheme for wireless power transfer systems using magnetic resonant coupling," *IEEE Transactions on Power Electronics*, Vol. 30, No. 7, 3998–4008, Jul. 2015.

[9] Li, H., J. Fang, S. Chen, K. Wang, and Y. Tang, "Pulse density modulation for maximum efficiency point tracking of wireless power transfer systems," *IEEE Transactions on Power Electronics*, Vol. 33, No. 6, 5492–5501, Jun. 2018.

[10] Li, H., S. Chen, J. Fang, and K. Wang, "Frequency-modulated phase shift keying communication for MEPT control of wireless power transfer," *IEEE Transactions on Power Electronics*, Vol. 36, No. 5, 4954–4959, May 2021.

[11] Chowdhury, S. A., S.-W. Kim, S.-M. Kim, J. Moon, I.-K. Cho, and D. Ahn, "Automatic tuning receiver for improved efficiency and EMI suppression in spread-spectrum wireless power transfer," *IEEE Transactions on Industrial Electronics*, Vol. 70, No. 1, 352–363, Jan. 2023.

[12] Fu, N., J. Deng, Z. Wang, and D. Chen, "An LCC–LCC compensated WPT system with switch-controlled capacitor for improving efficiency at wide output voltages," *IEEE Transactions on Power Electronics*, Vol. 38, No. 7, 9183–9194, Jul. 2023.

[13] Matsumoto, R., T. Fujita, and H. Fujimoto, "Communicationless reactance compensation using PWM-controlled switched capacitors for wireless power transfer," *IEEE Transactions on Power Electronics*, Vol. 38, No. 10, 13 194–13 206, Oct. 2023.

[14] Cai, C., S. Wu, L. Jiang, Z. Zhang, and S. Yang, "A 500-W wireless charging system with lightweight pick-up for unmanned aerial vehicles," *IEEE Transactions on Power Electronics*, Vol. 35, No. 8, 7721–7724, Aug. 2020.

[15] Li, Z., H. Liu, Y. Tian, and Y. Liu, "Constant current/voltage charging for primary-side controlled wireless charging system without using dual-side communication," *IEEE Transactions on Power Electronics*, Vol. 36, No. 12, 13 562–13 577, Dec. 2021.

[16] Wang, W., C. Xu, C. Zhang, and J. Yang, "Optimization of transmitting coils based on uniform magnetic field for unmanned aerial vehicle wireless charging system," *IEEE Transactions on Magnetics*, Vol. 57, No. 6, 1–5, Jun. 2021.

[17] Ann, S. and B. K. Lee, "Analysis of impedance tuning control and synchronous switching technique for a semibridgeless active rectifier in inductive power transfer systems for electric vehicles," *IEEE Transactions on Power Electronics*, Vol. 36, No. 8, 8786–8798, Aug. 2021.

[18] Li, Z., B. Xie, Y. Zhu, M. Tang, H. Liu, X. Guo, and H. Sun, "Wireless charging constant power output system based on LCC/SS self-switching," *IEEE Access*, Vol. 10, 86 435–86 444, 2022.

[19] Lu, J., G. Zhu, D. Lin, S.-C. Wong, and J. Jiang, "Load-independent voltage and current transfer characteristics of high-order resonant network in IPT system," *IEEE Journal of Emerging and Selected Topics in Power Electronics*, Vol. 7, No. 1, 422–436, Mar. 2019.

[20] Cai, J., X. Wu, P. Sun, Q. Deng, J. Sun, and H. Zhou, "Design of constant-voltage and constant-current output modes of double-sided LCC inductive power transfer system for variable coupling conditions," *IEEE Transactions on Power Electronics*, Vol. 39, No. 1, 1676–1689, Jan. 2024.

[21] Mishra, D., B. Singh, and B. K. Panigrahi, "Bi-directional EV charging with robust power controlled adaptive phase-shift algorithm," *IEEE Transactions on Vehicular Technology*, Vol. 72, No. 12, 15 491–15 501, Dec. 2023.

[22] Huang, Z., B. Zou, Z. Huang, H. H.-C. Iu, and C. K. Tse, "A single-stage IPT converter with optimal efficiency tracking and constant voltage output against dynamic variations of coupling and load," *IEEE Transactions on Transportation Electrification*, Vol. 11, No. 1, 1582–1592, Feb. 2025.

[23] Wang, L., P. Sun, Y. Liang, L. He, X. Wu, and Q. Deng, "Research on the control strategy of communication-free IPT system based on multiparameter joint real-time identification," *IEEE Transactions on Power Electronics*, Vol. 39, No. 1, 1912–1926, Jan. 2024.

[24] Zheng, Z., Y. Ma, Z. Wu, X. Cao, Q. Zhao, and J. Bai, "Research on constant current output control of wireless power transmission system based on parameter identification," *Progress In Electromagnetics Research C*, Vol. 152, 33–41, 2025.

[25] Kavimandan, U. D., S. M. Mahajan, and C. W. V. Neste, "Analysis and demonstration of a dynamic ZVS angle control using a tuning capacitor in a wireless power transfer system," *IEEE Journal of Emerging and Selected Topics in Power Electronics*, Vol. 9, No. 2, 1876–1890, Apr. 2021.

[26] Song, K., Z. Li, J. Jiang, and C. Zhu, "Constant current/voltage charging operation for series-series and series-parallel compensated wireless power transfer systems employing primary-side controller," *IEEE Transactions on Power Electronics*, Vol. 33, No. 9, 8065–8080, Sep. 2018.

[27] Wang, H., J. Sun, and K. W. E. Cheng, "A compact and integrated magnetic coupler design with cross-coupling elimination utilizing LCC-S compensation network for building attached photovoltaic systems," *IEEE Transactions on Magnetics*, Vol. 59, No. 11, 1–5, Nov. 2023.

[28] Li, S., W. Li, J. Deng, T. D. Nguyen, and C. C. Mi, "A double-sided LCC compensation network and its tuning method for wireless power transfer," *IEEE Transactions on Vehicular Technology*, Vol. 64, No. 6, 2261–2273, Jun. 2015.

[29] Wang, Z. B., D. Qiu, B. Zhang, W. Xiao, Y. Chen, and F. Xie, "Three-coil wireless power transfer system with constant output power and constant transfer efficiency characteristics," *Proceedings of the CSEE*, Vol. 42, No. 20, 7332–7343, 2022.

[30] Hu, Z., Y. Qiu, L. Wang, and Y.-F. Liu, "An interleaved llc resonant converter operating at constant switching frequency," *IEEE Transactions on Power Electronics*, Vol. 29, No. 6, 2931–2943, Jun. 2014.

[31] Zhao, J., J. Zhang, and Y. Zhu, "A flexible wireless power transfer system with switch controlled capacitor," *IEEE Access*, Vol. 7, 106 873–106 881, 2019.